Texas A&M University
Mechanical Engineering Department
Turbomachinery laboratory

Parameter Identification of an End Sealed SFD Part II: Improved Predictions of Added Mass Coefficients for Grooved SFDs and Oil Seals.

Research Progress Report to the Turbomachinery Research Consortium

TRC-SFD-2-07

Luis San Andrés
Mast-Childs Professor
Principal Investigator

Adolfo Delgado
Research Assistant

May 2007

TRC Project 32513/1519C3

Executive Summary

Added mass coefficients are not adequately predicted for SFD configurations including grooves or other recesses. This deficiency also extends to grooved floating ring oil seals operating under laminar flow conditions. In oil seals, the grooves are intended to reduce the cross-coupled stiffness coefficients and improve the seal stability characteristics. However, experimental results demonstrate that inner grooves do not reduce the force coefficients as much as accepted theory predicts. Furthermore, predictive codes for this type of seal do not account for fluid inertia effects, while experiments render large added mass coefficients.

A bulk-flow model is proposed to analyze multiple-groove SFD or oil seal configurations. A perturbation analysis yields zeroth and first order flow equations defined at each individual flow region (land and grooves) of constant clearance (c). At the groove regions, an effective groove depth (d_η) and clearance ($c_\eta = d_\eta + c$) are defined based on qualitative observations of the laminar flow pattern through annular cavities. This depth may differ from the actual physical groove depth. Boundary conditions between adjacent flow regions impose continuity of the pressure and flow fields. The boundary conditions at the inlet and exit planes are a function of the geometric configuration. Integration of the resulting dynamic pressure fields on the journal surface yields the force coefficients (stiffness, damping and inertia).

The predictive model indicates that the damping and stiffness coefficients decrease rapidly with increasing effective groove depths (d_η). Damping is roughly proportional to $1/c_\eta^3$. On the other hand, the added mass coefficient, which is proportional to $1/c_\eta$, is less sensitive to changes in the effective groove depth. Furthermore, predictions show that the added mass coefficient increases as the effective groove depth increases until it reaches a maximum value and starts decaying. Comparisons of the predicted and experimental force coefficients on a grooved oil seal and a SFD show excellent correlation over a narrow range of effective groove depths. Specifically, for a short and shallow mid-land groove in the test oil seal, predictions of added mass, cross-coupled stiffness, and damping coefficients correlate well with experimental data when using a fraction (1/2 or less) of the actual groove depth. Most importantly, current predictions, as well as the test

results, indicate that the inner groove in the oil seal does not isolate the adjacent film lands.

For SFD with a side feeding groove, prediction of damping and added mass coefficients also correlate well with test data for a narrow range of effective inlet groove depths. Future work will include further validation of the model with available experimental data and CFD analysis to determine the effective groove depths from the path of the streamline dividing the thru-flow and recirculation regions at the grooves.

Table of Contents

List of Tables

List of Figures

Nomenclature

C	Direct damping coefficient [N.s/m]
c	Clearance [m]
c_g	Groove clearance ($d_g + c$) [m]
c_η	Effective groove clearance ($d_\eta + c$) [m]
d_g	Groove depth [m]
d_η	Effective groove depth [m]
$(f,g)_{X,Y}$	Dynamic pressure functions [Pa]
h	Film thickness [m]
L	Axial length [m]
k_{xy}, k_{yx}	Cross-coupled stiffness coefficient [N/m]
$k_{x,z}$	Shear flow factors
M	Added mass coefficient [Kg]
$\dot{m}_{x,z}$	Mass flow rates [kg/s]
N	Number of flow regions
P	Pressure [Pa]
P_X, P_Y	First-order pressure field [Pa]
i	Imaginary number ($\sqrt{-1}$)
R	Journal radius [m]
$\overline{\mathrm{Re}}_*$	Modified squeeze film Reynolds number
s	Zeroth order pressure axial gradient [Pa/m]
t	Time [s]
V_x, V_z	Bulk flow velocities [m/s]
X,Y,Z	Inertial coordinate system [m]
x,z	Circumferential and axial coordinates [m]
Δe	Displacement amplitude [m]
μ	Absolute viscosity [Pa.s]
Ω	Rotor rotational speed [rad/s]
ω	Rotor whirling frequency [rad/s]
ρ	Oil density [kg/m^3]
θ	Angular coordinate [deg]
Subscripts	
0	Zeroth order solution
exp.	Derived from experiments
g	groove
N	Last annular cavity section
model	Derived from predictions
α	α-th annular cavity section

I Introduction

SFDs were originally analyzed as journal bearings using the classical Reynolds equation neglecting both the temporal and convective fluid inertia terms. Kuzma [1], in early 1967, demonstrates that fluid inertia effects should be considered in squeeze film dampers. In 1975, Reinhart and Lund [2], in a classical paper, derived the force coefficients for journal bearings including fluid inertia effects. The authors indicate that the added fluid mass term is relatively small for conventional journal bearings but it may be significant in long bearings or squeeze film dampers. A year later, Brennen [3] presents an analysis to determine the fluid forces for the flow in an annulus surrounding a long whirling cylinder under the assumption of laminar flow. The results evidence the importance of the fluid added mass effect on the dynamic response of the test system. In 1983, Tichy [4] uses an order of magnitude analysis to demonstrate that fluid inertia forces are indeed comparable to viscous forces in squeeze film dampers for Reynolds numbers equal to 10. In the early 80's extensive work was conducted by several researchers [3-9] to investigate the influence of fluid inertia effects on the dynamic response of SFDs. These analytical efforts to study fluid inertia effects have been partially successful. Predictions of fluid inertia coefficients present adequate correlation with experimental data only for the simplest geometries tested [6]. In the case of configurations with feeding grooves and recesses (mainly shallow ones), added mass coefficient are largely underpredicted by about 50% [6]. As a consequence, analytical efforts concentrated on studying the influence of circumferential grooves in the forced response of SFDs. Up to date, the added mass terms on SFDs remain to be properly predicted for most common geometries, as evidenced in recent experimental work [14]. Such deficiency also extends to grooved annular oils seals (floating rig seals) operating in the laminar flow regime [15].

The following review introduces some of the most relevant analytical work on fluid inertia effects on grooved SFD and oil seals, as well as some of the most recent experimental investigations evidencing large discrepancies between added mass predictions and test results.

II Literature Review

This section presents a brief review of research conducted to quantify the effect of fluid inertia on the dynamic response of grooved SFDs and annular oil seals, as well as experimental work exposing the discrepancy between predictions of added mass coefficients and test results. The publications in each subsection are presented in chronological order.

I.1 Grooved SFDs

San Andrés [16] analyzes the forced response of a squeeze film damper with a central groove. The analysis, based on the short length bearing model and for small centered journal motions, includes the dynamic interaction of the flow at the interface between the squeeze film lands and a central (mid-plane) feeding groove. Analytical results show that a SFD with a shallow groove behaves at low frequencies as a single land damper. Dynamic force coefficients are determined to be frequency dependent. Predictions show that the combined action of fluid inertia and groove volume-liquid compressibility affects the force coefficients for dynamic excitation at large frequencies.

Arauz and San Andrés [17] use bulk flow equations, as in Ref. [16], but include circumferential flow (i.e. no short length bearing assumption) and neglect fluid compressibility at the groove. The bulk flow equations for small centered journal orbits are amenable to be solved exactly. Predictions of tangential and radial forces at the groove and the SFD lands are compared to experimental results. Interestingly enough, recorded dynamic pressure levels at shallow grooves ($c_g/c < 10$) and the film land are of the same order of magnitude. Comparisons with experimental data indicate that the predictions reproduce well the forces at the groove, but underestimate the radial force and overestimate the tangential (damping) force at the damper film land.

Arauz and San Andrés [18] present tests revealing the importance of a circumferential feeding groove and recirculation annuli on the forced response of a test damper. The test results show that the radial forces in a groove with depth-to-clearance ratios of 5 to 10 are similar or larger to those at the SFD land (depending on the journal whirl orbit amplitude). For uncavitated lubricant conditions, the tangential (damping) forces at the groove are smaller than at the damper film land but still of comparable magnitude.

Zhang and Roberts [19] present an analysis to predict SFD force coefficients including the effects of the central groove and oil supply system. The authors make a balance of the flow and pressure starting at the upstream supply pipe, passing through a recirculation groove, and into the damper film land. Predictions are presented in terms of damping and inertia force coefficients, which are compared with experimental values obtained by Ellis *et al.* [20] and Zhang *et al.* [21]. The comparisons show that the derived formulas marginally improve the prediction of damping and inertia force coefficients. The analysis focuses more on modeling the inlet pipe line than the flow transition between the groove and the damper film land. An expression for the pressure drop at the groove-film land interface is obtained by using the inertialess axial velocity profile and integrating the axial momentum and continuity equations across the film thickness.

Qingchang *et al.* [22] analyze the effect of circumferential grooves on the forced response of SFDs. For the groove, the authors used the same model as that in Ref. [16]. For the squeeze film land the authors use a similar approach to that in Ref. [23]. The solution of the pressure field and fluid forces along the SFD follow form the continuity equation and equating the pressures at the interface groove-film land. Nonetheless, the experimental results show that the radial (inertial) force is underpredicted by a factor of three.

Della Pietra and Adilleta [12,13] present a comprehensive review of the state of the art on SFDs up to 2002. The review discusses the analytical and experimental investigations on fluid inertia effects on grooved SFDs, and urges for better models to predict force coefficients on SFDs with common geometries (i.e. including circumferential grooves and recesses).

Lund *et al.* [24] present analytical predictions and experimental results of dynamic force coefficients of a SFD with a central groove and sealed at both ends with O-rings. An equivalent first-order Reynolds equation is derived and solved using a perturbation analysis for small amplitude centered journal orbits. A bulk flow model is used to describe the conditions in the central groove. The experiments consist of unidirectional dynamic load excitations on SFDs with various groove depths and widths. The results show that the damping coefficient fairly agrees with analytical predictions for increasing groove volumes (i.e. depth and width). On the other hand, the fluid inertia force coefficient tends to be overpredicted (up to 70 %) as the groove volume increases.

Kim and Lee [25] present experiments and predictions of the force coefficients in a sealed SFD with feed and discharge grooves. The theoretical development follows from the bulk flow equations with the pressure and velocity fields as originally given by Mulcahy [5] and San Andrés [6]. The dynamic film pressure at the groove is obtained as in Ref. [16] where the fluid at the groove is regarded as slightly compressible. The tests and analysis includes one-stage and two-stage seal configurations. For the two-stage seal, predictions of the inertia coefficient correlate well experimental data, while the test damping coefficients are underestimated.

Recently, in 2006, San Andres and Delgado [14] experimentally identify force coefficients on an end sealed SFD describing circular centered orbits. The SFD is fed from a side plenum, and incorporates circumferential grooves at the inlet and outlet of the damper. The experimental work aims to evaluate the effectiveness of the end seal in preventing air ingestion and extract the force coefficient from single frequency excitation tests. The identified damping coefficients are presented as a function of the amplitude of motion and correlate well with predictive formula found in the literature [26]. On the other hand, the added mass coefficients are largely underpredicted. Interestingly enough, the authors state that more realistic predictions, correlating well with experimental estimations, are obtained using twice the length of the damper film land. This report provides a detailed analysis to support the improved correlations.

I.2 Grooved oil seals

The literature in annular liquid seals is extensive but mainly includes seals operating under turbulent flow regimes (i.e. $Re \geq 2000$). For the current analysis, the case of interest is grooved oil seals operating under laminar flow regimes. Oil seals are known to induce instability problems in compressors [27, 28]. A general practice is to groove the oil seals to reduce the cross-coupled stiffness coefficients and to improve their stability characteristics. This literature review includes analytical and experimental work conducted on grooved oil seals under laminar flow operation. In particular, the review emphasizes the correlation between predictions and experiments for added mass coefficients (i.e. fluid inertia effects).

Semanate and San Andrés [15] present an analysis to predict force coefficients of a grooved oil seal operating under either laminar or turbulent flow regimes. The analysis includes the solution of the isoviscous, bulk flow equations disregarding fluid inertia

terms. The analysis accounts for inertial and viscous loss effects at the seal entrance but neglects pressure variations across the circumferential grooves. Predictions indicate that the grooved oil seal cross-coupled stiffness and direct damping coefficients are significantly smaller that those of smooth seals. Such results indicate that the grooves effectively separate the seal lands and thus reduce the seal force coefficients. For example, for a seal with a single mid-land groove the code predicts that the cross-coupled stiffness and damping coefficients would be ¼ of those identified for the smooth seal. As mentioned above, fluid inertia effects in the lands are considered negligible in the noted reference.

Baheti and Kirk [27] obtain the pressure and temperature distributions in a grooved oil seal from a finite element solution of the Reynolds and energy equations. The study includes square and circular grooves with and without steps. The groove depths are approximately 6 times the seal clearance and the lengths are nearly 1/6 of the seal land length. Predictions indicate that the grooves effectively isolate the seal lands as the stiffness and damping force coefficients are reduced by approximately 60 % for the grooved configurations.

Childs *et al.* [28] identify experimentally the rotordynamic force coefficients and leakage characteristics of a smooth and a grooved oil seals operating in the laminar flow regime. The grooved seal includes three small round circumferential grooves. This research work is intended to provide experiments to validate predictions and to assess the effectiveness of the grooves in reducing cross-coupled stiffness effects. The experimentally derived force coefficients for the smooth seal are compared to predictions based on Ref. [29], and the grooved seal force coefficients are compared to predictions from Semante and San Andrés [30]. The experimental force coefficients for the smooth seal present reasonable agreement with the predictions based on [29] except for the added mass terms which are underpredicted by a factor of ~seven. The authors attribute the discrepancy to the effects of inlet groove and the exit chamber. However, pressure measurements at both the inlet groove an exit cavity show no pressure oscillations. On the other hand, predictions based on [30] do not represent well the experimental results from the grooved seal. The measurements do not reflect the large reduction in cross-coupled stiffnesses as predicted in [27, 30]. The current analysis hereby presented demonstrates that the exit (discharge) groove does not have an effect on the added mass

term, and that regardless of the groove depth, the groove will not isolate adjacent film lands.

Childs *et al.* [31] present more experiments on a grooved annular seal to determine the influence of the groove depth on the seal forced response and leakage performance. In this case, the test seal includes an internal single square groove. The groove depth-to clearance ratios tested are 5, 10 and 15. The tests include centered and off-centered journal operation up to 70 % of the radial clearance; rotor speeds from 4000 to 10000 rpm, and three oil supply pressures (24, 45, 70 bar). The Reynolds numbers for each case are well below 2000 (i.e. laminar flow condition). The results from the dynamic load tests indicate that the rotordynamic coefficients decrease with increasing groove depths except for the added mass terms. Comparisons of experimental data with predictions based on Ref. [30] show that the seal force coefficients are underpredicted, which indicates that the groove does not effectively separate the seal lands (i.e. K_{xy} (1 land) ≠ ¼ K_{xy} (2 lands), C_{xx}(1 land) ≠ ¼ C_{xx}(2 lands)). In addition, the test added mass coefficients are considerably large, up to 30 kg for centered journal operation. Predictions of added mass coefficients from Ref. [2] yield 2.8 kg (i.e. 10 times smaller than the experimental value).

III Analysis

As presented in the literature review, there is a need for a model that properly predicts inertia force coefficients on grooved SFDs and oil annular seals. The bulk flow model presently advanced is supported by qualitative observations of the laminar flow pattern through annular cavities with grooves. Figure 1 depicts a representation of the streamlines for a pressure driven flow on a symmetric annular cavity with a supply groove and a mid-land groove.

The analysis considers two major assumptions for determining the appropriate boundary conditions to obtain the fluid forces for small journal dynamic motions. The first assumption considers an effective groove clearance ($c_\eta = d_\eta + c$) defined by the streamline dividing the recirculation region from the rest of the thru-flow. Thus, the dividing streamline is assumed to act as a physical boundary defining an effective groove depth (d_η), obviously different from the physical groove depth.

In terms of damping coefficients, even for small effective groove depths (i.e. $d_\eta = 5c$), the damping contribution from the groove remains significantly lower than that related to

the ungrooved portion of the annular cavity. Recall that damping coefficients are proportional to $1/c_\eta^3$ [6]. On the other hand, the added mass coefficient, which is proportional to $1/c_\eta$ [6], presents the same order of magnitude at the grooves than at the lands (i.e. ungrooved portion) when based on a effective groove depth (d_η).

The second important assumption relates to the pressure distribution at the deep central groove. Initially, it was thought that there is no development of dynamic pressures at the central grooves in SFDs. However, experimental results [6,17,18] show that the dynamic pressures generated in a groove are of significant magnitude when compared to those generated at the film lands, in particular for motions about the journal centered condition. The generation of the dynamic pressure at the groove is related to the geometrical symmetry of the system and the large local squeeze film Reynolds number ($\rho\omega c_g^2/\mu$). For journal dynamic displacements the axial flow through the oil inlet plane must be zero, and thus the dynamic pressure field is not null at the groove.

A perturbation analysis of the bulk flow equations for centered small amplitude orbits implementing the aforementioned hypotheses follows.

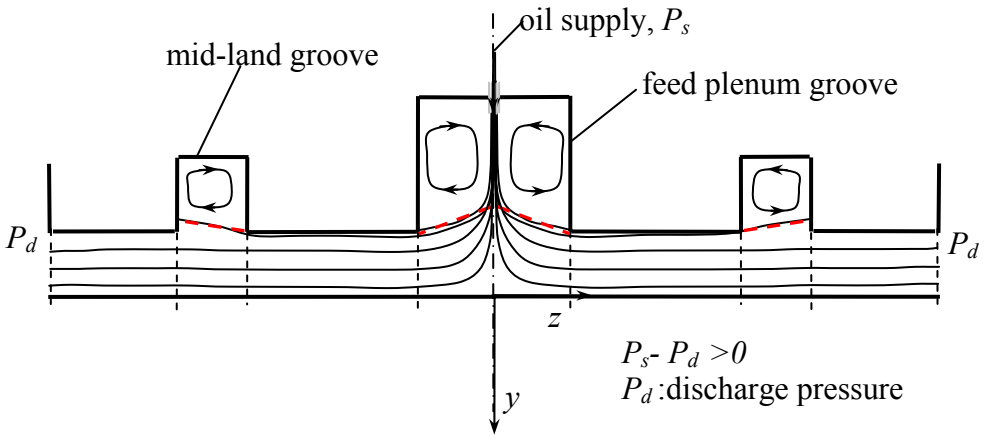

Figure 1 Schematic view of streamlines in axially symmetric grooved annular cavity ($\Delta P = P_s - P_d$).

III.1 Bulk flow formulation

The analysis determines the fluid forces developed in multi-groove annular cavities enclosing a rotating journal whirling with small amplitudes about a centered position. The model applies to SFDs with multiple constant clearance sections, and to smooth and grooved oil seals operating on the laminar flow regime. Specifically, the formulation is

detailed for the case of annular cavities with axially symmetric groove arrangements, including a central feeding groove as shown in Figure 2.

The multiple groove annular cavity is divided into individual flow regions with uniform clearance. In case of a groove, the depth is expressed in terms of an effective groove depth (d_η), which differs from the actual physical groove depth.

The following derivation applies to each individual flow region with constant clearance, and with the coordinate system set at the entrance of the corresponding grooved or ungrooved region. Figure 3 depicts the journal and the coordinate system used in the analysis for small journal motions about a centered position.

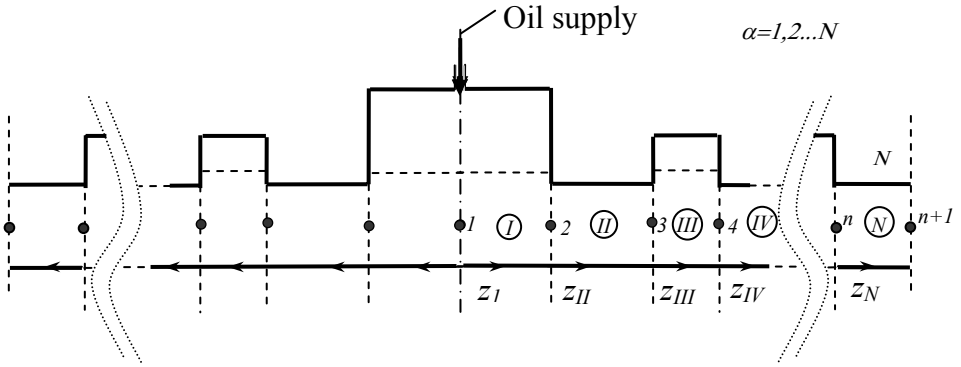

Figure 2 Schematic view of grooved annular cavity divided into flow regions.

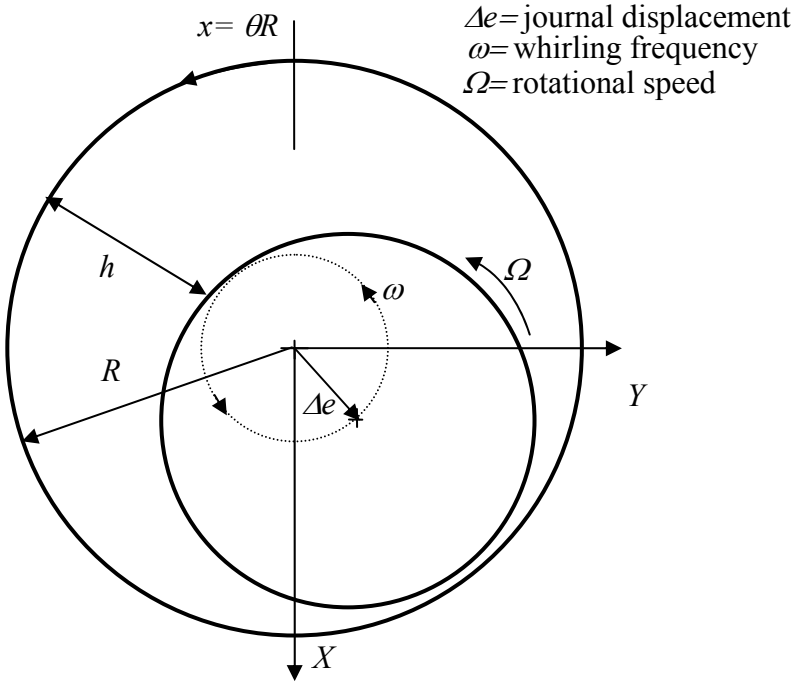

Figure 3 View of rotating and whirling journal and coordinate system for bulk-flow analysis.

Within each individual flow region the bulk-flow mass flow rates in the circumferential (x) and axial (z) directions are:

$$\dot{m}_{x_\alpha} = \rho h_\alpha V_{x_\alpha} \; ; \; \dot{m}_{z_\alpha} = \rho h_\alpha V_{z_\alpha} \qquad \alpha = I, II, ...N \tag{1}$$

where h_α is the film thickness, ($V_{x_\alpha}, V_{z_\alpha}$) are bulk-flow velocities for each flow region α, and ρ is the lubricant density.

The bulk-flow continuity and moment transport equations **without fluid advection terms** are linear and given as [32]:

$$\frac{\partial}{\partial x}\left(\dot{m}_{x_\alpha}\right) + \frac{\partial}{\partial z_\alpha}\left(\dot{m}_{z_\alpha}\right) + \frac{\partial}{\partial t}\left(\rho h_\alpha\right) = 0 \tag{2}$$

$$-h_\alpha \frac{\partial P_\alpha}{\partial x} = k_x \frac{\mu}{h_\alpha}\left(V_{x_\alpha} - \frac{\Omega R}{2}\right) + \frac{\partial\left(\dot{m}_{x_\alpha}\right)}{\partial t} \tag{3}$$

$$-h_\alpha \frac{\partial P_\alpha}{\partial z_\alpha} = k_z \, \mu \frac{V_{z_\alpha}}{h_\alpha} + \frac{\partial\left(\dot{m}_{z_\alpha}\right)}{\partial t} \; ; \qquad \alpha = I, II, ...N \tag{4}$$

with k_x=k_z=12 for laminar flow and μ is the lubricant viscosity. Equations (3) and (4) are written as:

$$\begin{aligned} \dot{m}_{x_\alpha} &= -\frac{\rho h_\alpha^{\,3}}{k_x \mu}\frac{\partial P_\alpha}{\partial x} - \frac{\rho h_\alpha^{\,2}}{k_x \mu}\frac{\partial\left(\dot{m}_{x_\alpha}\right)}{\partial t} + \frac{\rho h_\alpha \Omega R}{2}; \\ \dot{m}_{z_\alpha} &= -\frac{\rho h_\alpha^{\,3}}{k_z \mu}\frac{\partial P_\alpha}{\partial z_\alpha} - \frac{\rho h_\alpha^{\,2}}{k_z \mu}\frac{\partial\left(\dot{m}_{z_\alpha}\right)}{\partial t} \quad ; \quad \alpha = I, II, ...N \end{aligned} \tag{5}$$

Differentiating $\dot{m}_{x_\alpha}$ with respect to x, and $\dot{m}_{z_\alpha}$ with respect to z_α, adding both equations and disregarding second order terms yields a Reynolds-like equation for the film pressure of an incompressible fluid [33]

$$\frac{\partial}{\partial x}\left(h_\alpha^{\,3}\frac{\partial P_\alpha}{\partial x}\right)+\frac{\partial}{\partial z_\alpha}\left(h_\alpha^{\,3}\frac{\partial P_\alpha}{\partial z_\alpha}\right)=12\,\mu\frac{\partial}{\partial t}\left(h_\alpha\right)+6\mu R\Omega\frac{\partial}{\partial x}\left(h_\alpha\right)+\left(\rho\, h_\alpha^{\,2}\right)\frac{\partial^2}{\partial t^2}\left(h_\alpha\right) \qquad \alpha = I, II, ...N \tag{6}$$

The journal describes dynamic motions of small amplitude $(\Delta e_X\ ,\ \Delta e_Y\ ) << c_{\eta_\alpha}$ and frequency ω about its centered position,. The film thickness (h_α) equals

$$h_\alpha = c_{\eta_\alpha} + e^{i\omega t}\ \left\{\Delta e_X\ \cos(\theta)\ +\ \Delta e_Y \sin(\theta)\right\}; \Delta e_X, \Delta e_Y << c_{\eta_\alpha}\ , i\ =\sqrt{-1}; \alpha = I, II, ...N \tag{7}$$

where $c_{\eta_\alpha} = c + d_{\eta_\alpha}$ at a grooved region, of effective groove depth d_{η_α}. The pressure is expressed as a superposition of a zeroth order field (P_o) and a first order (dynamic) fields $(P_{X_\alpha}, P_{Y_\alpha})$

$$P_\alpha = P_{0_\alpha} + e^{i\omega t}\ \left\{\Delta e_X\ \ P_{X_\alpha}\ +\ \Delta e_Y\ P_{Y_\alpha}\right\}\ \ ;\ \ \alpha = I, II, ...N \tag{8}$$

Substitution of Eqs. (7) and (8), into Eq. (9) gives the zero$_{th}$ order equilibrium pressure equations

$$\frac{\partial}{\partial x}\left(c_{\eta_\alpha}^3\frac{\partial P_{0_\alpha}}{\partial x}\right)+\frac{\partial}{\partial z_\alpha}\left(c_{\eta_\alpha}^3\frac{\partial P_{0_\alpha}}{\partial z_\alpha}\right)\ =0\ \rightarrow\ \ \frac{d^2}{d\,z_\alpha^{\,2}}\left(P_{0_\alpha}\right)=0\rightarrow\ \ P_{0_\alpha}=a_\alpha+s_\alpha\, z_\alpha \qquad \alpha = I, II, ...N \tag{9}$$

since the static component of film thickness does not change along the axial or circumferential directions

The first order equations for journal displacements along the X and Y directions are

$$\frac{\partial^2 P_{X_\alpha}}{\partial x^2}+\frac{\partial^2 P_{X_\alpha}}{\partial z_\alpha^{\,2}}=12\,i\frac{\mu\omega}{c_{\eta_\alpha}^3}\left\{1+i\,\overline{\mathrm{Re}}_{*_\alpha}\right\}\cos(\theta)-\left\{\frac{6\mu\Omega}{c_{\eta_\alpha}^3}\right\}\sin(\theta)$$

$$\frac{\partial^2 P_{Y_\alpha}}{\partial x^2}+\frac{\partial^2 P_{Y_\alpha}}{\partial z_\alpha^{\,2}}=12\,i\frac{\mu\omega}{c_{\eta_\alpha}^3}\left\{1+i\,\overline{\mathrm{Re}}_{*_\alpha}\right\}\sin(\theta)+\left\{\frac{6\mu\Omega}{c_{\eta_\alpha}^3}\right\}\cos(\theta)\qquad ;\qquad \alpha = I, II, ...N \tag{10}$$

respectively, where $\overline{\mathrm{Re}}_{*_\alpha}=\dfrac{\rho\omega c_{\eta_\alpha}^2}{12\,\mu}$ is a modified local squeeze film Reynolds number,

The perturbed pressure field P_{X_α} is simply

$$P_{X_\alpha}(z) = f_{X_\alpha}(z_\alpha)\cos(\theta) + g_{X_\alpha}(z_\alpha)\sin(\theta) \quad ; \quad \alpha = I, II, ...N \tag{11}$$

Substituting Eq. (11) into the first of Eqs. (10) and collecting similar terms leads to

$$\begin{aligned} &\frac{d^2 f_{X_\alpha}}{d z^2} - \frac{f_{X_\alpha}}{R^2} = 12\, i \frac{\mu \omega}{c_{\eta_\alpha}^3}\left\{1 + i\,\overline{\mathrm{Re}_{*_\alpha}}\right\}; \\ &\frac{d^2 g_{X_\alpha}}{d z^2} - \frac{g_{X_\alpha}}{R^2} = -\frac{6\mu\Omega}{c_{\eta_\alpha}^3} \quad ; \quad \alpha = I, II, ...N \end{aligned} \tag{12}$$

The homogenous solutions of Eqs.(12) are:

$$\begin{aligned} &f_{X_{H_\alpha}}(z_\alpha) = c_{f_\alpha}\cosh\left(-z_\alpha / R\right) + s_{f_\alpha}\sinh\left(z_\alpha / R\right) \\ &g_{X_{H_\alpha}}(z_\alpha) = c_{g_\alpha}\cosh\left(-z_\alpha / R\right) + s_{g_\alpha}\sinh\left(z_\alpha / R\right); \quad \alpha = I, II, ...N \end{aligned} \tag{13}$$

with particular solutions:

$$f_{X_{P_\alpha}} = -12\, i \frac{\mu \omega R^2}{c_{\eta_\alpha}^3}\left\{1 + i\,\overline{\mathrm{Re}_{*_\alpha}}\right\} \quad ; \quad g_{X_{P_\alpha}} = -\frac{6\mu\Omega R^2}{c_{\eta_\alpha}^3} \tag{14}$$

Then, $f_{X_\alpha}(z_\alpha) = f_{X_{H_\alpha}}(z_\alpha) + f_{X_{P_\alpha}}$ and $g_{X_\alpha}(z_\alpha) = g_{X_{H_\alpha}}(z_\alpha) + g_{X_{P_\alpha}}$.

A similar procedure is to be followed for evaluation of P_{Y_α} where

$P_{Y_\alpha} = f_{Y_\alpha}(z_\alpha)\cos(\theta) + g_{Y_\alpha}(z_\alpha)\sin(\theta)$; and from Eq. (10) $g_{Y_\alpha} = f_{X_\alpha}$; $f_{Y_\alpha} = -g_{X_\alpha}$

The total dynamic fluid film force generated along the annular cavity includes the contribution of the forces generated at each flow region L_α (i.e. film lands and grooves). The total force (radial and tangential) is defined as

$$-\begin{bmatrix} K_{XX} - \omega^2 M_{XX} + \mathrm{i}\omega C_{XX} \\ K_{YX} - \omega^2 M_{YX} + \mathrm{i}\omega C_{YX} \end{bmatrix} = 2\sum_{\alpha=1}^{N}\int_0^{L_\alpha}\int_0^{2\pi R}\left\{\begin{Bmatrix} f_{X_\alpha}(z_\alpha)\cos(\theta)^2 \\ g_{X_\alpha}(z_\alpha)\sin(\theta)^2 \end{Bmatrix} dx\right\} dz_\alpha = 2\sum_{\alpha=1}^{N}\begin{Bmatrix} \pi R\int_0^{L_\alpha} f_{X_\alpha}(z_\alpha)\, dz_\alpha \\ \pi R\int_0^{L_\alpha} g_{X_\alpha}(z_\alpha)\, dz_\alpha \end{Bmatrix} \tag{15}$$

with $\alpha=1,2,...N$, and N as the number of flow regions. Note that $K_{XX}=K_{YY}$, $C_{XX}=C_{YY}$, $K_{XY}=-K_{YX}$ for centered motions.

From Eqs. (5), the volumetric flow rates, per unit length are

$$\begin{aligned}\dot{q}_{x_\alpha} &= \frac{\dot{m}_{x_\alpha}}{\rho} = -\frac{h_\alpha{}^3}{k_x\,\mu}\frac{\partial P_\alpha}{\partial x} - \frac{h_\alpha{}^2\,\rho}{k_x\,\mu}\frac{\partial\left(\dot{q}_{x_\alpha}\right)}{\partial t} + \frac{h_\alpha}{2}\Omega R;\\ \dot{q}_{z_\alpha} &= \frac{\dot{m}_{z_\alpha}}{\rho} = -\frac{h_\alpha{}^3}{k_z\,\mu}\frac{\partial P_\alpha}{\partial z} - \frac{h_\alpha{}^2\rho}{k_z\,\mu}\frac{\partial\left(\dot{q}_{z_\alpha}\right)}{\partial t}; \qquad \alpha = I, II, ...N\end{aligned} \tag{16}$$

As with the pressure field, the flow rates are defined as the superposition of zero$_{th}$ and first order flow fields, i.e.

$$\begin{aligned}\dot{q}_{x_\alpha} &= \dot{q}_{x_{0_\alpha}} + e^{i\omega t}\ \left\{\Delta e_X\ \dot{q}_{x_{X_\alpha}} + \Delta e_Y\ \dot{q}_{x_{Y_\alpha}}\right\};\\ \dot{q}_{z_\alpha} &= \dot{q}_{z_{0_\alpha}} + e^{i\omega t}\ \left\{\Delta e_X\ \dot{q}_{z_{X_\alpha}} + \Delta e_Y\ \dot{q}_{z_{Y_\alpha}}\right\}; \quad \alpha = I, II, ...N\end{aligned} \tag{17}$$

and

$$\begin{aligned}\frac{\partial \dot{q}_{x_\alpha}}{\partial t} &= e^{i\omega t}\, i\,\omega\ \left\{\Delta e_X\ \dot{q}_{x_{X_\alpha}} + \Delta e_Y\ \dot{q}_{x_{Y_\alpha}}\right\};\\ \frac{\partial \dot{q}_{z_\alpha}}{\partial t} &= e^{i\omega t}\, i\,\omega\ \left\{\Delta e_X\ \dot{q}_{z_{X_\alpha}} + \Delta e_Y\ \dot{q}_{z_{Y_\alpha}}\right\}; \qquad \alpha = I, II, ...N\end{aligned} \tag{18}$$

Substitution of Eqs. (7), (8) and (9) into Eq. (18) leads to zero$_{th}$ and first order expressions, i.e.

$$\dot{q}_{x_{X_\alpha}}\left(1+i\,\overline{\mathrm{Re}}_{*_\alpha}\right) = -\frac{c_{\eta_\alpha}^3}{12\,\mu}\frac{\partial P_{X_\alpha}}{\partial x} + \frac{\Omega R}{2}\cos(\theta); \quad \dot{q}_{x_{Y_\alpha}}\left(1+i\,\overline{\mathrm{Re}}_{*_\alpha}\right) = -\frac{c_{\eta_\alpha}^3}{12\,\mu}\frac{\partial P_{Y_\alpha}}{\partial x} + \frac{\Omega R}{2}\sin(\theta) \tag{19a}$$

$$\dot{q}_{z_{X_\alpha}}\left(1+i\,\overline{\mathrm{Re}}_{*_\alpha}\right) = -\frac{c_{\eta_\alpha}^3}{12\,\mu}\frac{\partial P_{X_\alpha}}{\partial z_\alpha} - \frac{3\,c_{\eta_\alpha}^2\cos(\theta)}{12\,\mu}\ s; \quad \dot{q}_{z_Y}\left(1+i\,\overline{\mathrm{Re}}_{*_\alpha}\right) = -\frac{c_{\eta_\alpha}^3}{12\,\mu}\frac{\partial P_{Y_\alpha}}{\partial z_\alpha} - \frac{3\,c_{\eta_\alpha}^2\sin(\theta)}{12\,\mu}\ s_\alpha \quad ;\ \alpha = I, II...N \tag{19b}$$

For motion perturbations along the X-direction,

$$\begin{aligned}\dot{q}_{z_{X_\alpha}}\left(1+i\,\overline{\mathrm{Re}}_{*_\alpha}\right) &= -\frac{c_{\eta_\alpha}^3}{12\,\mu}\frac{\partial P_{X_\alpha}}{\partial z_\alpha} - \frac{3\,c_{\eta_\alpha}^2\cos(\theta)}{12\,\mu}\ s_\alpha =\\ &-\frac{3\,c_{\eta_\alpha}^2\cos(\theta)}{12\,\mu}\ s_\alpha - \frac{c_C^3}{12\,\mu}\left[\frac{df_{X_\alpha}}{dz_\alpha}\cos(\theta) + \frac{dg_{X_\alpha}}{dz_\alpha}\sin(\theta)\right]; \qquad \alpha = I, II, ...N\end{aligned} \tag{20}$$

The various coefficients $(c_{f_\alpha}, c_{g_\alpha}, s_{f_\alpha}, s_{g_\alpha})_{\alpha=I,II,..N}$ are obtained from appropriate boundary conditions at the interfaces groove-film lands, and from specified pressure or flow conditions at the inlet and exit planes of the global flow region. The pressure must be single-valued and the axial flow rates, leaving one flow region and entering the next flow region, must be identical. In the case of a SFD, the rotational speed (Ω) is set to zero.

I.1.1 Boundary conditions

First, the static pressure field is defined using Eq.(9), provided that the supply (inlet) and discharge pressures ($P_{I,}$ P_{n+1}) are specified. Once the static pressure gradients are identified (i.e. $s_\alpha = \frac{dP_\alpha}{dz_\alpha}$), the dynamic pressure field (P_{X_α}) is obtained by applying the following boundary conditions:

a) The cavity exit discharges to ambient pressure and thus there is no generation of dynamic pressure at the exit plate (last flow region, z_N=L_N). This condition is written as

$$P_{X_N}\Big|_{z_N=L_N} = 0 = f_{x_N}(L_N)\cos(\theta) + g_{x_N}(L_N)\sin(\theta) \tag{21}$$

Separating the sine and cosine terms and substituting in Eq. (13) yields

$$\begin{aligned} &c_{f_N}\cosh\left(L_N/R\right) + s_{f_N}\sinh\left(L_N/R\right) = F_N \;;\; F_N = 12\,i\,\frac{\mu\,\omega\,R^2}{c_{\eta_N}{}^3} \\ &c_{g_N}\cosh\left(L_N/R\right) + s_{g_N}\sinh\left(L_N/R\right) = G_N \;;\; G_N = -\frac{6\mu\Omega R^2}{c_{\eta_N}{}^3} \end{aligned} \tag{22}$$

b) At interfaces groove and land, the first-order pressures are identical, i.e.

$$\begin{aligned} &P_{X_\alpha}\Big|_{z_\alpha=L_\alpha} = P_{X_{\alpha+1}}\Big|_{z_{\alpha+1}=0}; \quad \alpha = 1...N-1 \\ &\rightarrow \quad f_{X_\alpha}(L_\alpha) = f_{X_{\alpha+1}}(0); \;\; g_{X_\alpha}(L_\alpha) = g_{X_{\alpha+1}}(0) \end{aligned} \tag{23}$$

c) The axial flow rates must match at the interface between groove and land, i.e.

$$\dot{q}_{z_{X_\alpha}}\left(1 + i\,\overline{\mathrm{Re}}_{*_\alpha}\right)\Big|_{z_\alpha=L_\alpha} = \dot{q}_{z_{X_{\alpha+1}}}\left(1 + i\,\overline{\mathrm{Re}}_{*_{\alpha+1}}\right)\Big|_{z_{\alpha+1}=0}; \quad \alpha = 1...N-1 \tag{24}$$

Substituting in Eq. (13) yields

$$\frac{c_{\eta_\alpha}^3}{R}\left[c_{f_\alpha}\sinh\left(L_\alpha/R\right)+s_{f_\alpha}\cosh\left(L_\alpha/R\right)\right]-\frac{c_{\eta_{\alpha+1}}^3}{R}\left[s_{f_{\alpha+1}}\right]=-3c_{\eta_\alpha}^2\,s_\alpha+3c_{\eta_{\alpha+1}}^2\,s_{\alpha+1}$$

$$\frac{c_{\eta_\alpha}^3}{R}\left[c_{g_\alpha}\sinh\left(L_\alpha/R\right)+s_{g_\alpha}\cosh\left(L_\alpha/R\right)\right]-\frac{c_{\eta_{\alpha+1}}^3}{R}\left[s_{g_{\alpha+1}}\right]=0 \qquad (25)$$

d) Finally, due to geometrical symmetry, the axial flow rate must be null at $z_1=0$ (groove middle plane). Thus, from Eq. 25, $s_{g_1} = 0$. This last boundary condition implies a non-zero dynamic pressure value at the groove middle plane.

The combined set of boundary conditions provides the necessary equations to solve for the dynamic pressure functions and thus obtain the force coefficients.

First, the method is applied to determine the force coefficients of a simple one land SFD to validate the results with the classical formulas [2]. Subsequently, the application of these equations is illustrated for two cases: a grooved oil seal and an end sealed SFD.

III.2 Single film land- classical solution model

Figure 4 presents a schematic view of a single SFD land extending from $-L/2 \le z \le L/2$. Both ends are exposed to ambient pressure and there is no static axial pressure drop.

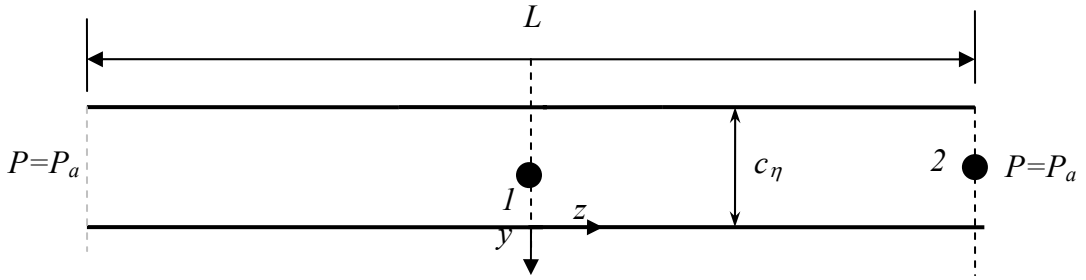

Figure 4 Schematic view of a simple SFD and boundary conditions.

The first order pressure fields must be symmetric about $z=0$; hence the hyperbolic sine terms disappear in Eq. (13), i.e. $s_f=s_g=0$. Thus

$$f_X(z)=c_{f_X}\cosh\left(z/R\right)+f_{X_p}\,;\quad g_X(z)=c_{g_X}\cosh\left(z/R\right) \qquad (26)$$

At the ends the pressure is ambient (P_a), and thus the dynamic pressure is set to zero at both ends, hence

$$P_X\big|_{z=\frac{L}{2}} = f_X\left(\frac{L}{D}\right)=0;\rightarrow\ c_f = {-f_{X_P}}\Big/{\cosh\left(L/D\right)};\ c_g=0 \tag{27}$$

with f_{X_P} defined in Eq.(14). Integrating the pressure across the damper land

$$K_{XX} - \omega^2 M_{XX} + \mathrm{i}\omega C_{XX} = -\pi R \int_{-L/2}^{L/2} f(z)\,dz = -f_P\,\pi R L\left[1-\frac{\tanh\left(L/D\right)}{\left(L/D\right)}\right] \tag{28}$$

yields the force coefficients

$$\begin{aligned} C_{XX} &= 12\pi\frac{\mu R^3 L}{c^3}\left[1-\frac{\tanh\left(L/D\right)}{\left(L/D\right)}\right] \\ K_{XX}&=0;\quad M_{XX} = \pi\frac{\rho R^3 L}{c}\left[1-\frac{\tanh\left(L/D\right)}{\left(L/D\right)}\right] \end{aligned} \tag{29}$$

which coincide with the classical damping and inertia force coefficients derived by Reinhart and Lund [2].

IV Model validation with experimental data

This section includes comparisons of experimental and predicted damping, stiffness and mass coefficients for an oil ring seal and an end sealed SFD. The results are presented in terms of an effective groove clearance ($c_\eta = d_\eta + c$), where d_η is the effective groove depth and c is the film land clearance.

IV.1 Grooved Oil Seal

The experimental data for the oil seal is obtained from Graviss [33]. Figure 5 depicts the actual configuration of the grooved oil seal. Notice that the test configuration is axially symmetric, with parallel seals and a central supply groove.

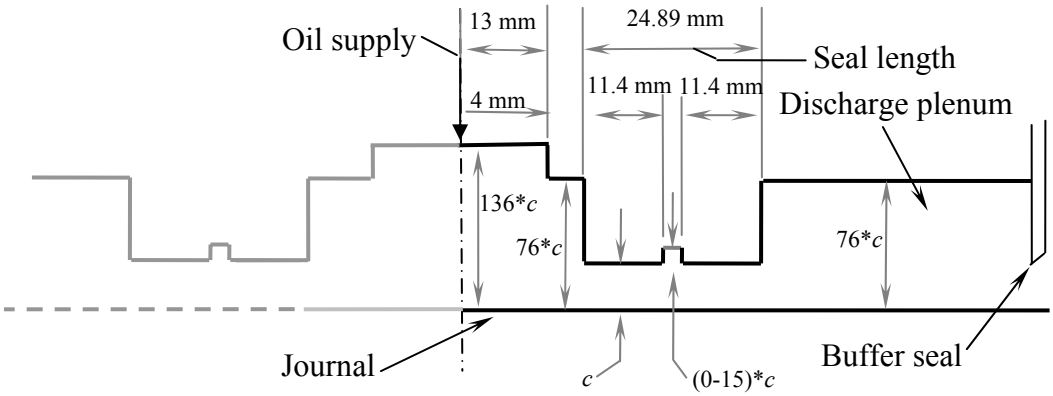

Figure 5 Configuration of parallel oil seals tested in [33].

IV.1.1 Geometry and model description

Figure 6 depicts the modeled portion of the oil seal and the partition into flow regions. Table 1 lists the physical dimensions, fluid properties and operating conditions of the test seal. The seal is divided into 4 flow regions with the following boundary conditions:

- Dynamic pressure set to zero at exit plane (Eq. 21).
- Pressures and flow rates equated at intermediate boundaries (Eqs. 23, 24)
- Axial flow rate at inlet groove (symmetry plane) is set to zero ($s_{g_1} = 0$)

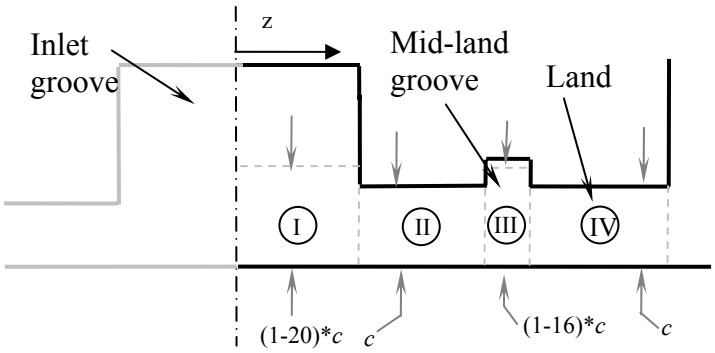

Figure 6 Partial view of test grooved oil seal geometry [33] and flow regions for predictions.

Table 1 Oil seal configuration, operating conditions and fluid properties.

Dimensions	
Journal Diameter	117 mm
Seal length	24.89 mm
Clearance	85.9 μm
½ Inlet groove length	17 mm
½ Inlet groove depth (d_{g_I})	135c
Mid-land groove length	2 mm
Mid-land groove depth ($d_{g_{III}}$)	(0,5,10,15)c (tests)
Parameters	
Shaft speed	4000 rpm -10000 rpm
Oil density	850 kg/m^3
Oil viscosity	0.02 Pa.s
Supply Pressure	2.4-7 bar

IV.1.2 Results and comparisons to experimental data

The dynamic pressure fields over each flow region are integrated to obtain the seal force coefficients as detailed in Eq. (15). Figure 7 presents the damping and added mass coefficients versus an effective inlet groove-to-seal clearance ratios for the seal configuration without mid-land (internal) groove (i.e. $c_{III} = c$). The results show that the damping coefficient (tangential force) rapidly converges to a constant value (C=88 kN.s/m) for $c_{\eta_I} \geq 10c$. For deep inlet grooves, the contribution of the groove to the overall tangential force (damping force) is negligible.

On the other hand, the direct added mass coefficient converges more slowly towards an asymptotic value. However, the most important observation is that the added mass coefficient presents good correlation with the experimental results precisely in the neighborhood of c_η magnitudes for which the overall damping becomes insensitive to the groove depth. Thus, comparisons of the damping values for decreasing d_η with that for a deep groove may be used to obtain an effective groove clearance c_η that properly predicts the mass coefficients. Of course, this recommendation applies to relatively large and deep (central) grooves.

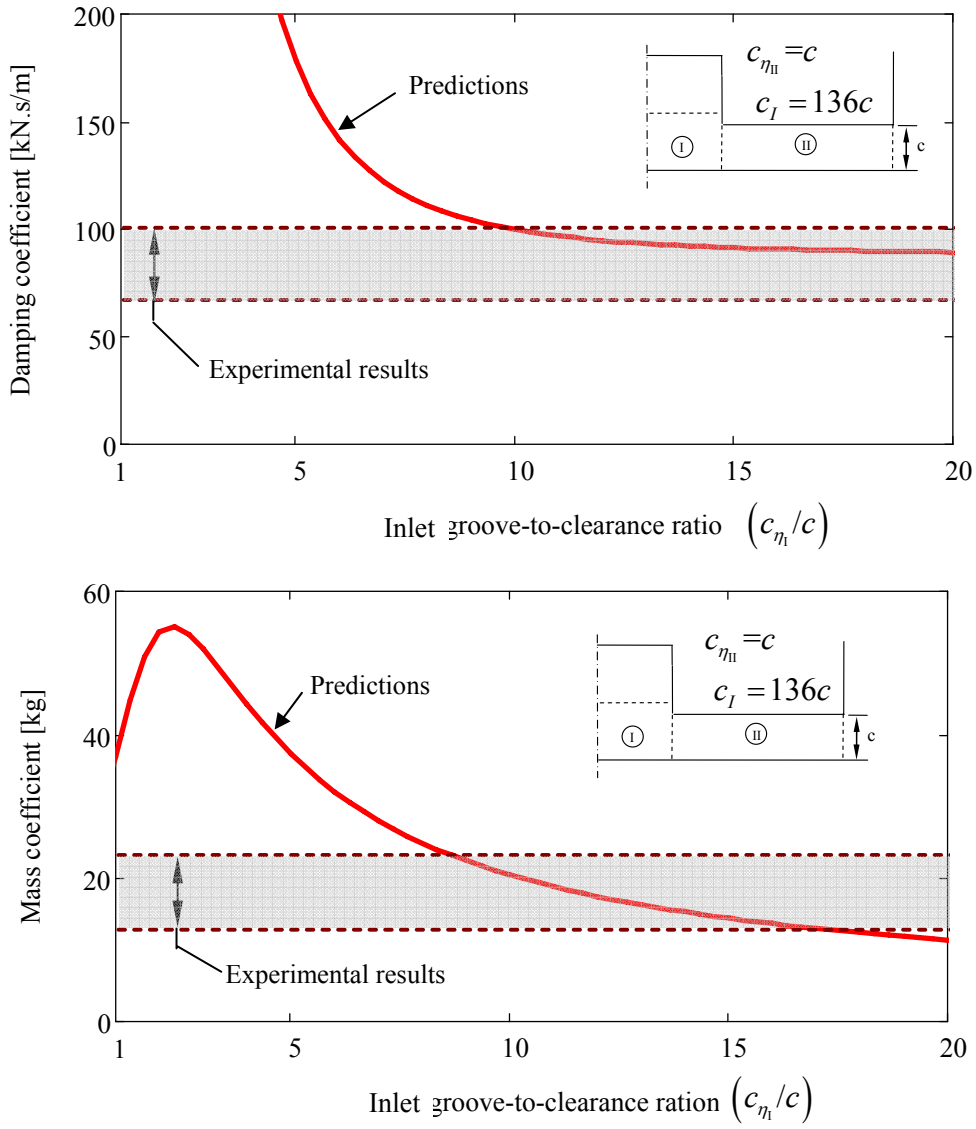

Figure 7 Direct damping and added mass coefficients versus effective inlet groove-to-seal clearance ratio. Solid lines represent predictions and dotted lines enclose the range of experimental values from [33] for a smooth seal (no mid-land groove).

For the configuration with an internal groove dividing the original seal length, Figure 8 presents the predicted damping and added mass coefficients versus effective inlet groove-to-seal clearance ratios. The graph includes three different mid-land grooves with effective groove depths ($d_{\eta_{III}}$=5c, 10c, 15c). The damping coefficient quickly decreases for increasing mid-land groove depths. On the other hand, the added mass coefficient increases as the effective groove depth increases up to a peak value (i.e. $d_{\eta_{III}}=5c$). As in the previous figure, the added mass coefficient correlates well with predictions for the

smallest c_η, i.e. 6c, that has a minimum impact on the overall tangential force developed by the seal.

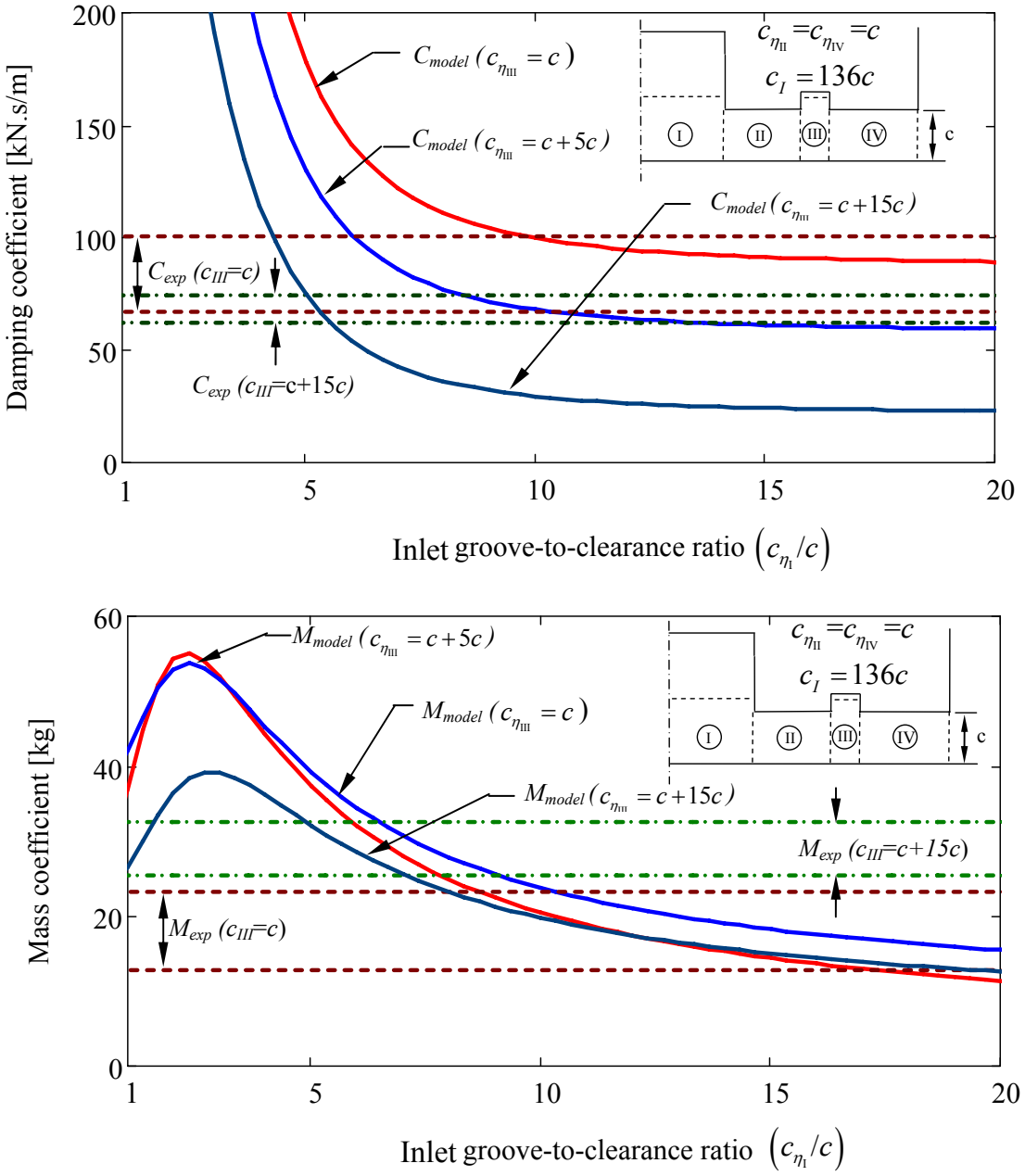

Figure 8 Direct damping and added mass coefficients versus effective central groove groove-to-clearance ratio. Solid lines represent predictions for three different effective mid-land seal groove depths $(d_{\eta_{III}}=5c,\ 10c,\ 15c)$ **. Dotted lines enclose the range of experimental values from [33] for two seal depths** $(d_{g_{III}}=c,\ c+15c)$ **.**

Figure 9 depicts the direct damping and added mass coefficients versus mid-land groove to-seal clearance ratios, including two effective groove depths for the central groove. These values are within the range of best correlation in Figure 8. The damping

steadily decreases as the mid-land groove effective depth ($d_{\eta_{III}}$) increases, whereas the mass presents a maximum value at $c_{\eta_{III}} \approx 5$. It is obvious that using the actual groove depth in the prediction would lead to smaller damping coefficients. In this case, the mid-land groove is relatively shallow and short when compared to the seal land and the central groove. For this mid-land groove, it seems that the best effective groove depth is around 1/3 of the physical depth. Thus, the results show that using a fraction of the groove depth (even ½) leads to much better predictions of added mass coefficients.

Although, the effective depth should depend on the groove actual length and depth, current predictions may be generalized to short and shallow mid-land grooves typically used in grooved oil seals. A more general correlation will be determined using further test comparisons and CFD calculations to determine the effective groove depth from the streamline dividing the thru-flow and recirculation region.

Figure 10 displays the cross-coupled stiffness coefficient (K_{xy}) versus rotor speed. The results include experimental data from Ref.[33] for no mid-land groove and with a mid-land groove 15c deep (i.e. c_{III}=16c). The predictions are based on an effective inlet groove depth (d_{η_I}) of 11c and a mid-land effective groove depth ($d_{\eta_{III}}$) of 6c (i.e. half of actual groove size). The predictions correlate best for the lowest rotor speeds. More importantly, the reduction in cross-coupled stiffness is properly captured using effective groove depths ($d_{\eta_{I,III}}$) that provide good correlation between experiments and predictions of added mass and damping coefficients.

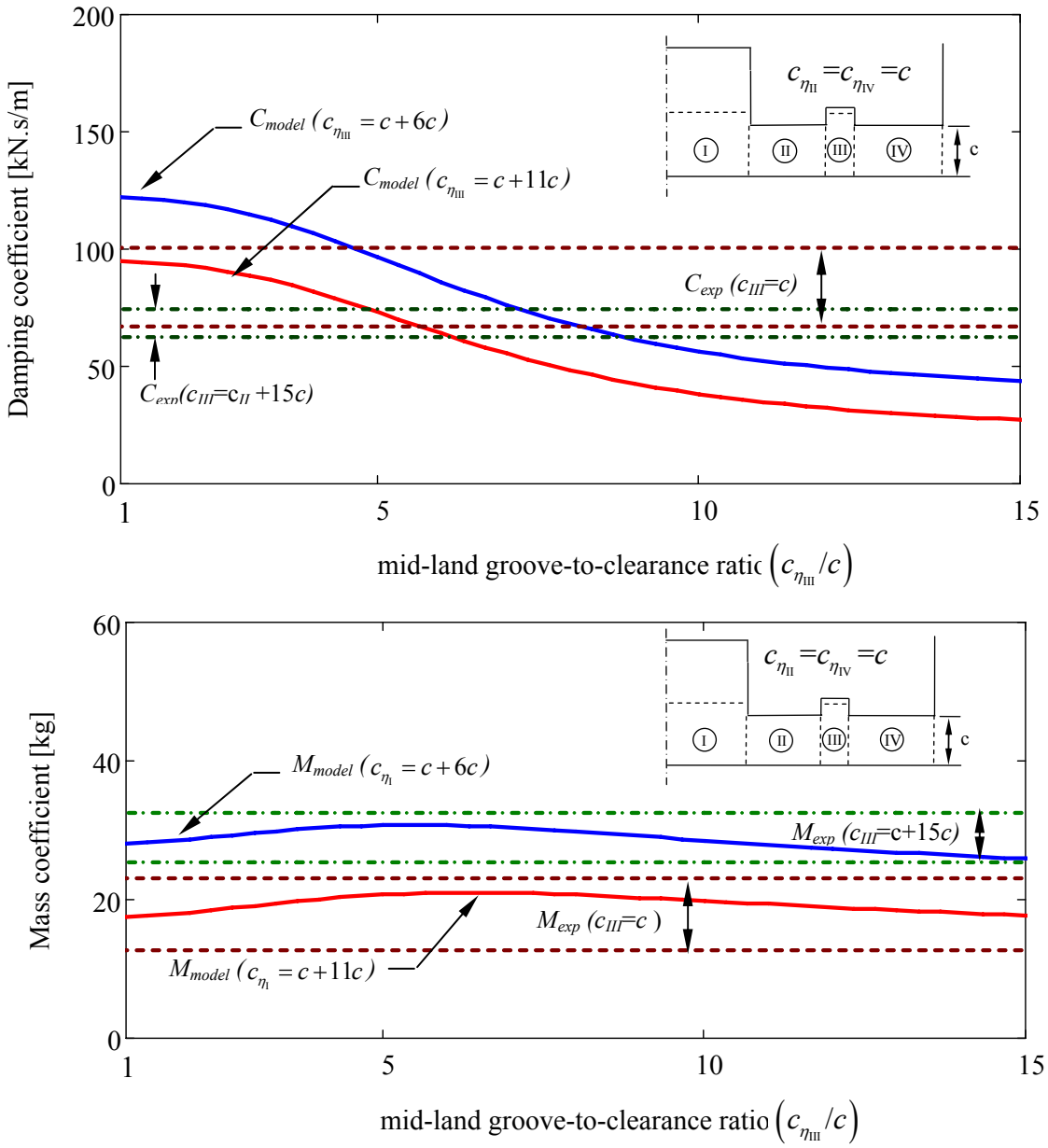

Figure 9 Direct damping and added mass coefficients versus effective mid-land groove depth. Solid lines represent predictions for two different effective central groove depths $(d_{\eta_1}=6c,\ 11c)$**. Dotted lines enclose the range of experimental values from [33] for two seal depths** $(d_{g_{III}}=0,\ 15c)$**.**

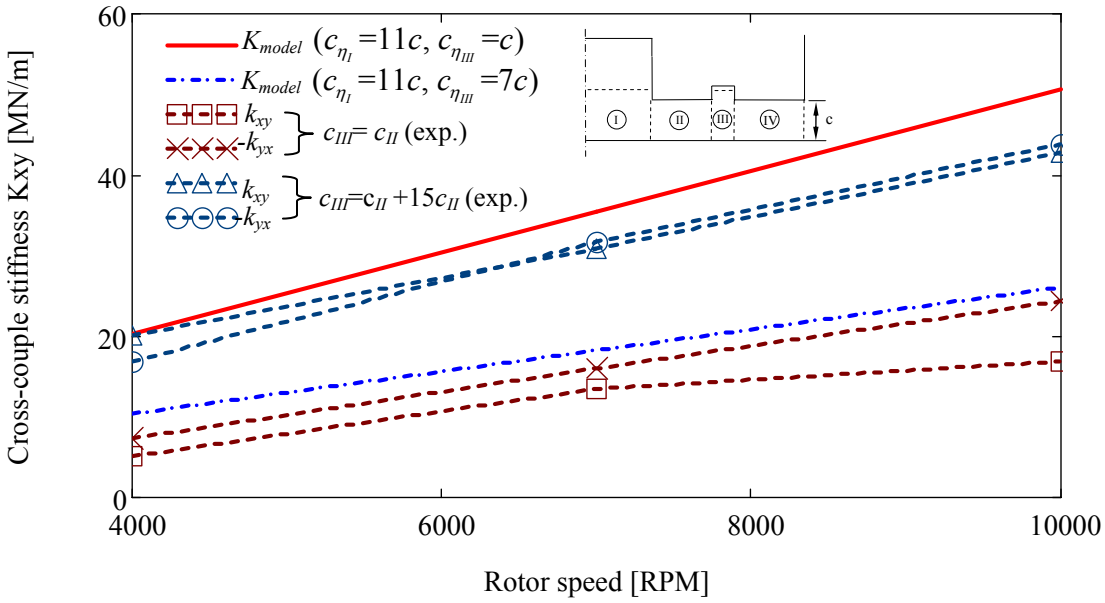

Figure 10 Cross-coupled stiffness coefficients versus rotor speed. Solid lines represent predictions for smooth seal and a effective mid-land groove depth with ($d_{\eta_{III}}$=0,6c). Dotted lines represent experimental values from [33] for a smooth seal and a grooved seal (mid-land groove depth =16c).

IV.2 Sealed SFD

In this section the model predictions are compared to experimental results obtained in a sealed SFD as part an experimental research sponsored by TRC [14].

IV.2.1 Geometry and model description

Figure 11 shows a cut view of the test SFD. The damper is fed from the top and the oils exists the damper at an end discharge groove and four outlet ports. Each outlet port includes a 2.8mm hole flow restrictor. Measurements of the dynamic pressure are available at the discharge groove. Figure 12 depicts a schematic view of the SFD detailing the groove and land dimensions, and the flow region subdivisions.

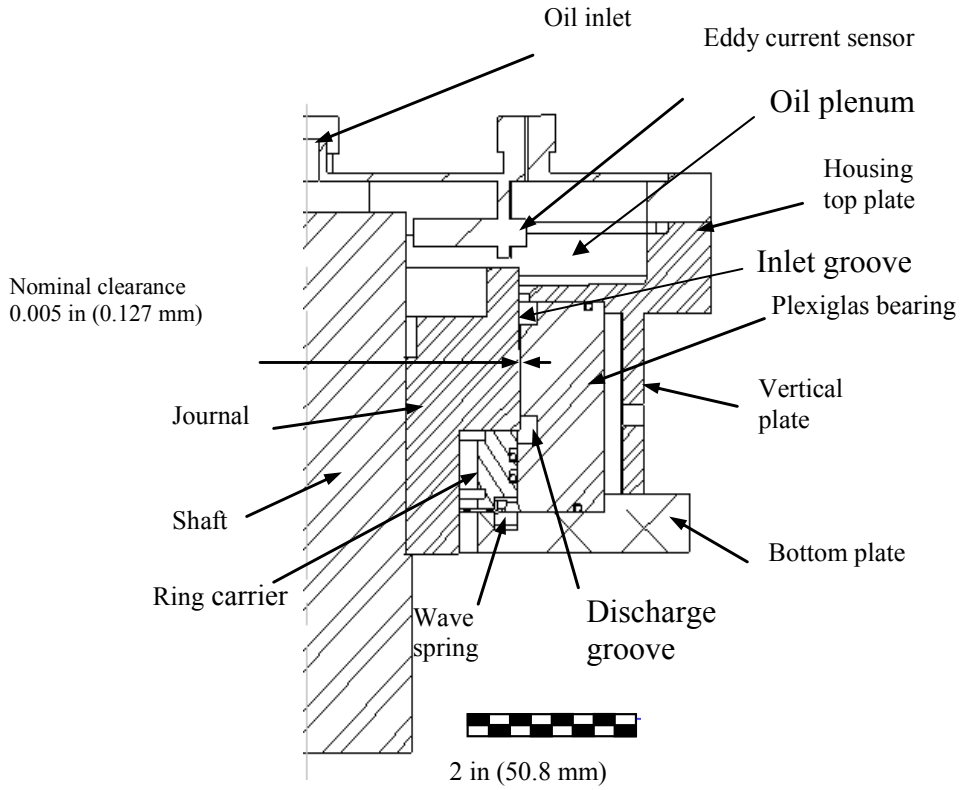

Figure 11 Sealed-end SFD assembly cut view.

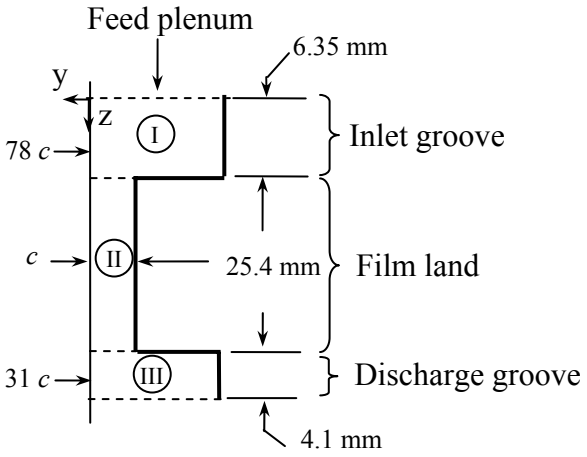

Figure 12 Test squeeze film damper geometry and flow regions used for predictions [14].

The boundary conditions are:

- Null axial flow at the feeding groove inlet (Eq. 21). This condition implies that the dynamic pressure in the plenum does not allow for backflow at the damper inlet.

- Equal pressure and flow rates at internal flow region interfaces. (Eqs. 23,24)
- Dynamic pressure amplitude set at outlet plane from measurements.

Table 2 Test conditions for dynamic load tests (CCO). Lubricated SFD

Inlet pressure (P_s)*	31 kPa
Discharge groove pressure (P_r)*	8.6 kPa-15.5 kPa
Frequency range	20-70 Hz (2 Hz step)
Lubricant temperature (T)	23-25 ^{0}C (73-77 ^{0}F)
Viscosity (η)	3.1 cP- 2.8 cP
Clearance (c)	125-127 μm (4.9-5 mils)
Orbit amplitude (e)	12-50 μm (0.5-2 mils)
Flow restrictors (hole diameter)	2.8 mm

*: Gauge pressure.

IV.2.2 Results and comparisons to experimental data

Figure 13 depicts the SFD damping and added mass coefficients versus effective discharge groove-to-film clearance ratios and two arbitrary effective inlet groove depths ($d_{\eta_I} = 11c, 6c$). The results show that both force coefficients are insensitive to an outlet groove depth of $d_{\eta_{III}} \geq 3c$. Thus, only the actual physical discharge groove depth is considered in the parametric study.

Figure 14 depicts the damping and added mass coefficients versus effective inlet groove-to-film clearance ratios. Regarding the inlet groove, the results are similar to those found for the oil seal (Figure 7). Again, the best estimates of mass coefficients correspond to the smallest effective groove depths (i.e. $c_{\eta_I} \sim 10c$) that do not have a significant impact (>10%) on the SFD tangential forces (damping coefficient) estimated using the actual groove depth.

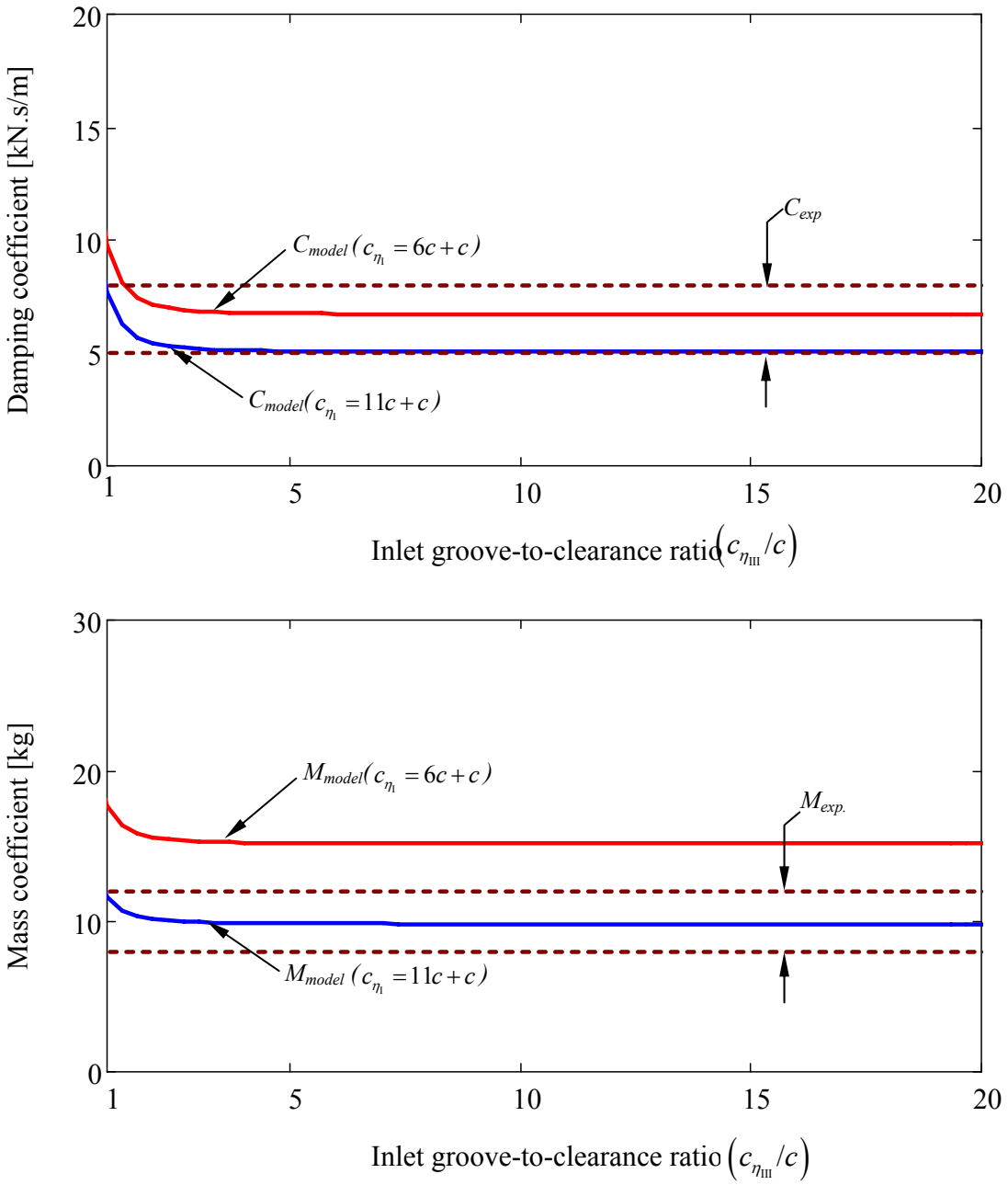

Figure 13 Predicted SFD damping and added mass coefficients versus effective inlet groove depths. Solid lines represent predictions for two different inlet effective groove depths $(c_{\eta_I} = 12c, 7c)$. Dotted lines represent range of experimental values from [14].

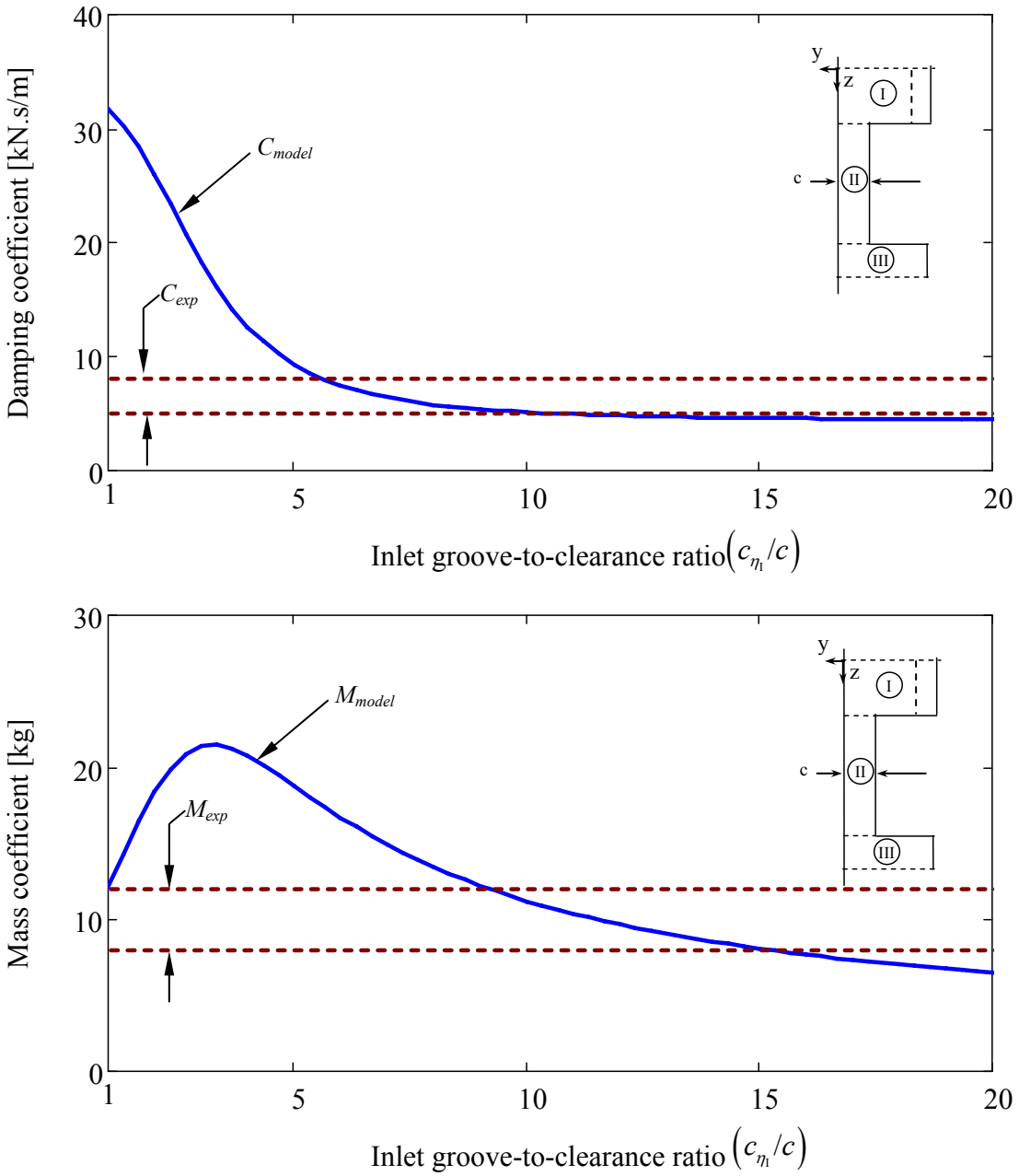

Figure 14 Predicted SFD added mass coefficient versus effective inlet groove depth. Solid lines represent predictions. Dotted lines represent range of experimental values from [14].

V Conclusions

An improved bulk-flow model to predict force coefficients in multiple groove annular cavities is presented. The model divides the multiple groove annular cavities into flow regions of constant clearance. At the groove regions, an effective groove depth (d_η) and clearance ($c_\eta = d_\eta + c$) are defined based on qualitative observations of the laminar flow pattern through annular cavities. Continuity of the pressure and axial flow field is imposed at the flow region interfaces. For a central groove, considering geometrical symmetry, the axial flow at the mid plane is set to zero. This observation is supported by experiments [6,17,18] that evidence the generation of relatively large dynamic pressures at grooves in SFDs. The predictive model reproduces the classical force coefficients (from Ref. [2]) for a single land SFD. Furthermore, the model shows that the damping and stiffness coefficients decrease rapidly with increasing effective groove depths as these are proportional to $1/c_\eta^3$. On the other hand, the added mass coefficient, which is proportional to $1/c_\eta$, is less sensitive to changes in the effective groove depth.

The model results explain unusual experimental data obtained in ring oil seals [33] and an end sealed SFD [14] through a parametric study varying the effective groove depths (d_η). Comparisons of predicted and experimental force coefficients show excellent correlation for a narrow range of effective groove depths. Most importantly, the parametric study shows that the best analytical correlation for the force coefficients is obtained for the minimum effective groove depths for which the overall damping is not substantially modified (<10%) from that calculated using the actual physical groove depth.

The seal cross-coupled stiffness coefficients are well predicted using an effective groove depth (d_η) that best predicts also damping and added mass coefficients. More importantly, unlike the existing models, this formulation effectively predicts (i.e. does not overpredict) the reduction of cross-coupled stiffness due to the addition of a mid-land groove.

In terms of a mid-land groove in a seal, the parametric study shows good correlation with the experimental data for effective depth (d_η) values smaller or equal to 50% of the groove depth. This result may be generalized for short and shallow grooves like those

found in oil seals. However, in order to determine the most appropriate effective depth for other groove sizes it is necessary to conduct more comparisons with experiments and to perform CFD calculations to find the effective groove depth from the streamline dividing the thru-flow from the recirculation region across the grooves. Future work will include such comparisons to determine appropriate effective depths according to the groove geometry.

VI References

[1] Kuzma, D. C., 1967, "Fluid Inertia Effects in Squeeze films," Appl. Scientific Research, **18**, pp.15-20.

[2] Reinhardt, F., and Lund, J. W., 1975, "The Influence of Fluid Inertia on the Dynamic Properties of Journal Bearings," ASME J. Lubr. Technol., **97**(1), pp. 154-167.

[3] Brennen, C., 1976, "On the Flow in an Annulus Surrounding a Whirling Cylinder," J. Fluid Mech., **75**(1), pp. 173-191.

[4] Tichy, J. A., 1983, "The Effect of Fluid Inertia in Squeeze Film Damper Bearings: A Heuristic and Physical Description," ASME Paper 83-GT-177..

[5] Mulcahy, T. M., 1980, "Fluid Forces on Rods Vibrating in Finite Length Annular Regions," Trans. ASME, **47**, pp. 234-246.

[6] San Andrés, 1985, "Effect of Fluid Inertia Effect on Squeeze Film Damper Force Response," Ph.D. Dissertation, December, Texas A&M University, College Station, TX.

[7] San Andrés, L., and Vance, J., 1986, " Effect of Fluid Inertia on Squeeze-Film Damper Forces for Small-Amplitude Circular-Centered Motions," ASLE Trans., **30**(1), pp. 63-68.

[8] Zhang J. X., and Roberts J. B., 1993, "Observations on the Nonlinear Fluid Forces in Short Cylindrical Squeeze Film Dampers," J. Tribol., **115**(3), pp. 692-698

[9] Zhang J. X., 1997, "Fluid Inertia Effects on the Performance of Short and Long Squeeze Film Dampers Execution Periodic Vibration," J. Tribol., **119**(3), pp. 306-314

[10] Qingchang, T., Wei, L., and Jun, Z., 1997, "Fluid Forces in Short Squeeze-Film Damper Bearings," Tribol. Int., **30**(10), pp. 733-738

[11] Zhang J. X.,1997, "Fluid Inertia Effects on the Performance of Short and Long Squeeze Film Dampers Execution Periodic Vibration," J. Tribol., **119**(3), pp. 306-314

[12] Della Pietra, L., and Adiletta, G., 2002,"The Squeeze Film Damper over Four Decades of Investigations. Part I: Characteristics and Operating Features," Shock Vib. Dig, **34**(1), pp. 3-26.

[13] Della Pietra, L., and Adiletta, G., 2002,"The Squeeze Film Damper over Four Decades of Investigations. Part II: Rotordynamic Analyses with Rigid and Flexible Rotors," Shock Vib. Dig., **34**(2), pp. 97-126.

[14] Delgado, A., and San Andrés, L., 2006, "Identification of Force Coefficients in a Squeeze Film Damper with a Mechanical Seal," TRC report, TRC-SFD-1-06, May.

[15] Semanate, J., and San Andrés, L., 1993, "Analysis of Multi-Land High Pressure Oil Seals," STLE Tribol. Trans., **36**(4), pp 661–669.

[16] San Andrés, L., 1992, "Analysis of Short Squeeze Film Dampers with a Central Groove," J. Tribol., **114**(4), pp. 659-665.

[17] Arauz, G., and San Andrés, L., 1994, "Effect of a Circumferential Feeding Groove on the Dynamic Force Response of a Short Squeeze Film Damper," J. Tribol., **116**(2), pp. 369-377.

[18] Arauz, G., and San Andrés L., 1996, "Experimental Study on the Effect of a Circumferential Feeding Groove on the Dynamic Force Response of a Sealed Squeeze

Film Damper," J. Tribol. ,**118**(4), pp 900-905

[19] Zhang J. X., and Roberts J. B.,1996, "Force Coefficients for a Centrally Grooved Short Squeeze Film Damper," J. Tribol., **118**(3), pp. 608-616

[20] Ellis, J., Roberts, J. B., and Hosseini, S. A., 1990, "The Complete Determination of Squeeze-Film Linear Dynamic Coefficients from Experimental Data," J. Tribol., **112**(4), pp. 712-724.

[21] Zhang, J., Roberts, J. B., and Ellis, J., 1994, "Experimental Behavior of a Short Cylindrical Squeeze Film Damper Executing Circular Centered Orbits," J. Tribol., **116**(3), pp. 528-534.

[22] Qingchang, T., Xaohua, L, and Dawei, Z., 1998, "Analytical Study of the Effect of a Circumferential Feeding Groove on the Unbalance Response of a Rigid Rotor in a Squeeze film Damper," Tribol. Int., **31**(5), pp. 265-270

[23] Tichy J. A. and Bou-Said B., 1991, Hydrodynamic Lubrication and Bearing Behavior with Impulsive Loads," ASLE Tribol. Trans., **34**(4), pp. 505-512**.**

[24] Lund, J., W., and Myllerup, C., M., Hartmann, H., 2003, "Inertia Effects in Squeeze-Film Damper Bearings Generated by Circumferential Oil Supply Groove," J. Vib. Acoust., **125**(4), pp. 495-499

[25] Kim, K. J., and Lee, C. W, 2005, "Dynamic Characteristics of Sealed Squeeze Film Damper with a Central Feeding Groove," J. Tribol., **127**(1), pp. 103-111.

[26] Zeidan, F.Y., San Andrés, L., and Vance, J. M., 1996, "Design and Application of Squeeze Film Dampers in Rotating Machinery," *Proc. 25th Turbomachinery Symposium*, Houston, TX, pp.169-188.

[27] Baheti, S., and Kirk, R., 1995, "Finite Element Thermo-Hydrodynamic Solution of Floating Ring Seals for High Pressure Compressors Using the Finite-Element Method," STLE Tribol. Trans.,**38**, pp. 86-97.

[28] Childs, D. W. Rodriguez, L. E., Cullotta, V., Al-Ghasem, A., and Graviss, M., 2006, "Rotordynamic-Coefficients and Static (Equilibrium Loci and Leakage) Characteristics for Short, Laminar-Flow Annular Seals," J. Tribol., **128**(2), pp. 378-387

[29] Zirkelback, N., and San Andrés, L., 1996, "Bulk-Flow Model for the Transition to Turbulence Regime in Annular Seals," STLE Tribol. Trans., **39**(4), pp. 835–842.

[30] Semanate, J., and San Andrés, L., 1993, "Thermal Analysis of Locked Multi-Ring Oil Seals," Tribol. Int., **27**, pp. 197-206.

[31] Childs, D. W., Graviss, M., and Rodriguez, L. E., 2007, "The Influence of Groove Size on the Static and Rotordynamic Characteristics of Short, Laminar-Flow Annular Seals," ASME J. Tribol, **129**(2), 398-406.

[32] San Andrés, L., "Modern Hydrodynamic Lubrication Theory," Tribology Group, Texas A&M University, http://phn.tamu.edu/me626. (accessed on 05/15/07)

[33] Graviss, M., 2005, "The Influence of a Central Groove on Static and Dynamic Characteristics of an Annular Liquid Seal with Laminar Flow," M.S. Thesis, Texas A&M Univ., College Station, TX.